RSC Advances

PAPER

View Article Online
View Journal | View Issue



Cite this: *RSC Adv.*, 2020, **10**, 35490

# A direct-write method for preparing a bimetal sulfide/graphene composite as a free-standing electrode for high-performance microsupercapacitors†

Hao Liu, Xiao-Juan Liu, Feng-Ying Dong and Xin-Zhi Sun *

It is a great challenge to ideally integrate graphene with its unique two-dimensional (2D) and porous structure into the pseudocapacitive materials. In this paper, a simple technique, *i.e.* direct-laser-writing (DLW), was developed to fabricate microsupercapacitors (MSCs) with excellent electrochemical performance, marked as Ni–Co–S/laser induced graphene (LIG) that exhibit a high areal specific capacitance of 680 mF $cm^{-2}$ at the current density of 1 mA $cm^{-2}$. A symmetric MSC device was assembled using Ni–Co–S/LIG as a positive electrode and active carbon (AC) as the negative electrode, and exhibited a high areal energy density of 56.9 μW h $cm^{-2}$ at the power density of 800 μW $cm^{-2}$, and excellent cycling stability maintaining 89.6% of the areal specific capacitance after 8000 cycles. The synergistic effect of bimetallic Ni–Co–S and the LIG with the 2D structure results in the excellent electrochemical performance. This work demonstrates a method to integrate Ni–Co–S pseudocapacitive materials into porous graphene with a direct-laser-writing technique. The produced integrated materials possess high energy density that can be used in MSCs.

Received 22nd July 2020
Accepted 5th September 2020

DOI: 10.1039/d0ra06376b

rsc.li/rsc-advances



## 1 Introduction

The fast development of modern microelectronics requires energy storage devices to be miniaturized.[1–6] It is well known that microbatteries are the most widely used miniaturized energy storage device, although they have limited life span as the main disadvantage.[2,3,8,9] Microsupercapacitors (MSCs), compared with microbatteries, perform better in terms of power density, lifespan, reversibility of redox reaction, *etc.*[3–10] It is a great challenge to design miniaturized MSCs with high energy density meanwhile maintaining electrochemical performance.[7,11] Furthermore, an in-plane structure is more desirable for application in MSCs, because it can provide microscale integrated circuits.[12,13]

In recent years, graphene-based nanomaterials have attracted great attention for their unique two-dimensional (2D) and porous structure.[13,14] However, commercialization of graphene-based nanomaterials is difficult due to its complicated, costly, and tedious process.[15–17] For example, graphene films were produced by using laser scribing of hydrated graphene oxide (GO) film, which showed predominant electrochemical performance.[18–21] But it is still difficult to synthesize GO into graphene film in large scale.[22,23] In recent years, a simple, fast and direct method is developed for the preparation of 2D porous graphene film from polymers by using direct-laser-writing (DLW) technique. Since then, the produced so-called laser-induced-graphene (LIG)[24] has been widely used in MSCs.[25–29]

The energy density of the supercapacitor device is determined by the specific capacitance and the voltage window ($E = CV^2/2$).[30] Therefore, in order to improve the energy storage, pseudocapacitive materials are loaded onto the graphene to offer pseudocapacitance from the redox reaction generated by metal ions. Recently, transition metal sulfide (TMS) electrode materials have attracted much attention due to their predominant pseudocapacity.[31–33] For example, the fabrication of cobalt-nickel-sulfide as electrode materials has been applied in improving supercapacitor performance owing to fast redox reactions, higher conductivity, diverse valence state and availability.[34] Pang and his group members state in detail the application of different sulfides in energy storage.[35] Compared with nonmetallic sulfide, the combination of nickel and cobalt in bimetal sulfide gives a wide voltage window and improves the energy storage performance.[36,37]

In this study, we developed a simple and one-step method towards preparation of bimetal nickel-cobalt-sulfide composite from the precursor, and LIG from the carbon cloth by using direct-laser-writing (DLW) technique. The bimetal Ni–Co–S/LIG exhibits an outstanding areal specific capacitance of 680 mF $cm^{-2}$ at the current density of 1 mA $cm^{-2}$, which is superior to

*College of Chemistry and Pharmaceutical Sciences, Qingdao Agricultural University, Qingdao 266109, China. E-mail: xzsun@qau.edu.cn*

† Electronic supplementary information (ESI) available. See DOI: 10.1039/d0ra06376b

the substrate LIG electrode materials. In addition, the asymmetric MSCs were fabricated with Ni–Co–S/LIG as positive electrode and active carbon (AC) as negative electrode materials, respectively. Moreover, the asymmetric MSCs device can reach a maximum energy density of 56.9 μW h $cm^{-2}$ at a power density of 800 μW $cm^{-2}$, which exceeds most of the reported asymmetric MSCs containing nickel or cobalt or LIG materials.

## 2 Experimental section

### 2.1 Materials synthesis

**2.1.1 The pretreatment of the substrate carbon cloth.** The substrate carbon cloth (CC) was further purified with 0.1 M HCl, acetone and ethanol under ultrasonic stirring for 10 min, respectively. And then, the carbon cloth was placed in a mould with 20 mm × 20 mm × 20 mm dimension.

**2.1.2 The preparation of the precursor.** The detailed experimental design is as followed. Firstly, the starch solution was prepared with 24 g starch dissolving in 60 mL deionized water, the solution was stirred at 65 °C until homogeneous.[38] Secondly, 2.33 g $NiCl_2 \cdot 6H_2O$, 0.048 g $CoCl_2 \cdot 6H_2O$ and 1.21 g L-cysteine were dissolved in 20 mL deionized water under stirring intensely, subsequently, 15 g of prepared-starch solution added. And then, 500 μL homogeneous solutions after stirring for 1 h was decanted to the pretreated carbon cloth in the mould. Lastly, the mould was placed in an oven at 60 °C for 8 h and the precursor was obtained.

**2.1.3 The preparation of Ni–Co–S/LIG.** The as-prepared precursor was directly written using a laser (10.6 μm, Epilog $CO_2$ Laser) scribing at a power of 6.0 W and Ni–Co–S/LIG was obtained. The laser scan rate was 9 mm $s^{-1}$, and auto-focusing was adopted for reducing the error of measuring laser *z*-distance. All experiments were conducted under room temperature and ambient air. The active material regions like Chinese character "凸" were got. In order to remove the unreacted precursors, all products were immersed in acetic acid solution (0.2 M) for 30 min, and washed with deionized water until pure composites were got.

### 2.2 Materials characterization

The surface morphologies of the as-prepared sample were analyzed by field-emission scanning electron microscopy (FESEM, Hitachi, Japan, JEOL-7500F). The elementary compositions and content were obtained using an Energy disperse X-ray spectroscopy equipment (EDS) (Oxford Instruments Isis 300 with voltage of 20 kV). The phase composition was measured on a Rigaku D/MAX-2500/PC at 40 kV with 70 mA Philips X'pert diffractometer equipped with Cu kα radiation ($\lambda$ = 1.5418 Å), with the $2\theta$ range from 10 to 80° at the scan rate of 0.50 $min^{-1}$. The interior and detailed morphology were investigated by HRTEM (FEI, Tecnai G2-F30) with an accelerating voltage of 300 kV. The crystal lattice data, namely, the selected area electron diffraction (SAED) was obtained by HRTEM.

X-ray photoelectron spectroscopy (XPS) was carried on a Thermo ESCALAB 250Xi device, which Al Kα X-ray beams was used as excitation source ($hv$ = 1486.6 eV). All the spectra were adjusted with C1s peaks at 284.5 eV as reference.

The crystalline size ($L_a$) in "*a*" axis was obtained from the different ratio of the intensity of the G peak ($I_G$) and D peak ($I_D$) using Raman spectroscopic data. The equation following was used to calculate the value of $L_a$.[24]

$$L_a = \left(2.4 \times 10^{-10}\right) \times {\lambda_1}^4 \times \left(\frac{I_G}{I_D}\right) \quad (1)$$

where the value of $\lambda_1$ is 532 nm, which is wavelength of the Raman laser.

### 2.3 Electrochemical measurements

The electrochemical measurements were carried on electrochemical workstation (CHI 760E, Shanghai) at room temperature. The single electrode materials were evaluated by a three-electrode system with 2 M KOH as the electrolyte, with platinum foil served as the counter electrode and AgCl/Ag electrode as the reference electrode.

The specific areal (CA, in mF $cm^{-2}$) capacitance of the negative electrode and device were obtained from the galvanostatic discharge graph at different densities according to the following formular.[24]

$$C_A = \frac{I \times \Delta t}{S \times \Delta V} = \frac{I}{S \times (dV/dt)} \quad (2)$$

where $I$ and $\Delta V$ is the discharge current (*A*) and time (s), respectively. $S$ is the active materials area ($cm^2$), which is 1 $cm^2$, and $\Delta V$ is the operating voltage (V) (reading from the discharge curve and need exclude the potential drop), and $d$ is the thickness of active materials. For the device used in experiment, $d$ was 360 μm.

Electrochemical impedance spectroscopy was performed using a sinusoidal signal with a frequency scope from 0.01 to $10^5$ Hz with a magnitude of 10 mV. The solution of resistance ($R_s$) was got with the voltage drop (in the beginning of the discharge curve) using the following equation.

$$R_S = \frac{V_{drop}}{2I} \quad (3)$$

where $I$ is the constant current (*A*).

The asymmetric MSCs device was built with Ni–Co–S/LIG as positive electrode and the commercial activate carbon (AC) as negative electrode, which were separated with the nonwovens separator (NKK-MPF 30AC-100, Japan) in 2 M KOH electrolyte.

To get the optimal electrochemical performance of asymmetric MSCs device, the charge balance of negative and positive should abide by the rule of following relationship $q+ = q-$. The charge storage in each electrode is related to the specific capacitance ($C$), the voltage window obtained from GCD curve ($\Delta V$) and the mass of the active materials ($m$), showing in the equation below[39]

$$q = C \times \Delta V \times m \quad (4)$$

Hence, the mass of AC was calculated according to the above-mentioned formula.

The AC electrode was fabricated according to the procedure as followed. The negative materials were composed of AC, the binder (such as polyvinylidene fluoride, PVDF) and acetylene black, with the mass ratio of 8 : 1 : 1, respectively. Firstly, AC and acetylene black were mixed uniformly by grinding, and then a drop of the solvent (such as 1-methyl-2-pyrrolidone) was added while maintaining the mixing until the homogeneous slurry was formed. Secondly, the slurry was painted on a piece of nickel foam (the painting area is about $1 \times 1$ cm$^2$), and the foam was pressed under 10 MPa for 1 min. Last, the nickel foam was dried at 80 °C for 12 h. The mass loading of the AC on nickel foam was 7.5–8.5 mg cm$^{-2}$. Compared to the AC, the contribution of the nickel foam is ignorable under the same measurement conditions.

The specific areal energy density and specific areal power density of the asymmetric MSCs device were obtained according to two equations shown below[24]

$$E_A = \frac{1}{2} C_A \frac{(\Delta V)^2}{3600} \quad (5)$$

$$P_A = \frac{E_A}{\Delta t} \times 3600 \quad (6)$$

where $E$ is the energy density ($E_A$, in μW h cm$^{-2}$), $P$ is the power density ($P_A$, in mW cm$^{-2}$), $I$ is the discharge current (A), $V$ (t) is the discharge potential excluding the potential drop, $A_s$ is the total area of the active materials regions including the nickel foam and carbon cloth, $\Delta V$ are the discharge time (s).

# 3 Result and discussion

## 3.1 Morphology and structural characteristics

The fabrication procedures of Ni–Co–S/LIG positive electrode on carbon cloth (CC) are schematically shown in Fig. 1. Firstly, the mixed homogeneous solutions have been prepared *via* the starch solution, Ni ion and Co ion solution were kept under magnetic stirring vigorously for 30 min. Consequently, 500 μL homogeneous solutions were dropped into the mould that carbon cloth was pretreated well in, and then were dried in the oven. The products with green colour were the precursor before written with the laser scribing. Secondly, the precursor was directly written using a $CO_2$ laser scribing and then the Ni–Co–S/LIG was obtained. The active material regions like Chinese character "凸" were got. During the scribing, the superhigh temperature makes CC undergo graphitization and promotes the nucleation course of Ni–Co sulfide, and Ni–Co–S/LIG hybrids were generated.[40]

The crystal structure and compositions of the as-prepared samples are characterized by X-ray diffraction (XRD), as shown in Fig. 2a. All diffraction peaks of $Ni_3S_2$/LIG are indexed to (110), (003), (202) and (113) plane reflections of rhombohedral phase $Ni_3S_2$ (JCPDS 044-1418). Except the peaks at 25.89° and 44.30° which are from the C·C substrate, other diffraction peaks of Ni–Co–S/LIG are indexed to cubic $Co_9S_8$ (JCPDS 003-0631) and rhombohedral phase $Ni_3S_2$ (JCPDS 044-1418). Obviously, the XRD patterns of Ni–Co–S/LIG differed from the XRD patterns of the carbon cloth and Ni–Co precursor as shown in Fig. S1.† The element compositions can also be confirmed by EDS analysis. As shown in Fig. 2c, Ni–Co–S/LIG consisted of five elements including C, Ni, Co, S and O. No diffraction peaks of oxide (MO, M = Ni or Co) can be observed in the XRD pattern of Ni–Co–S/LIG, which may indicate their low content or poor crystal structure. $Ni_3S_2$/LIG and $Co_9S_8$/LIG have been prepared by the same method under the same preparation condition with Ni–Co–S/LIG. As shown in Fig. S2a,† the XRD patterns of Ni–Co–S/LIG were the sum of that of $Ni_3S_2$/LIG and $Co_9S_8$/LIG. Fig. S2b† showed the XRD patterns with the different amount of Co mingling in the Ni–Co–S/LIG, indicating these four samples had the same composition.

The samples as-prepared were directly written using 10.6 μm $CO_2$ laser scribing. The existence of graphene can be confirmed by the Raman spectrum measurement. In the grapheme structure, the D, G and 2D bands associated with the edge defect, the highly ordered graphite and characteristic of few layer graphene, respectively.[41] As shown in Fig. 2b, three characteristic peaks of the D, G and 2D bands of LIG, starch-LIG and Ni–Co–S/LIG are appeared at 1350, 1580 and 2700 cm$^{-1}$ approximately (Table S1†), which indicates the presence of graphene. Obviously, the 2D band of Ni–Co–S/LIG is more intense than that of

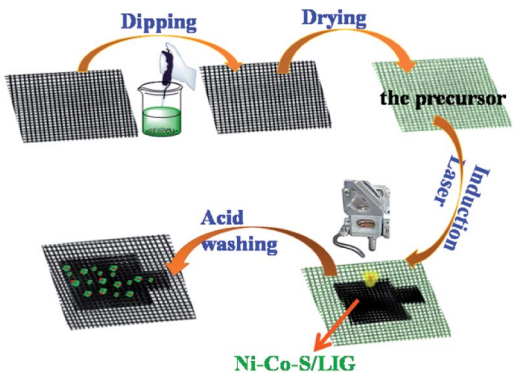


Fig. 1 Schematic illustration of the fabrication of Ni–Co–S/LIG electrode.

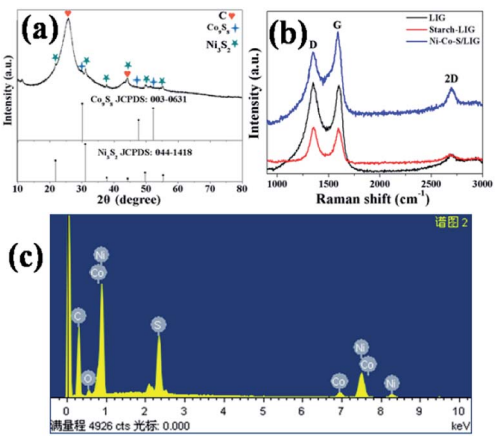


Fig. 2 The XRD pattern of Ni–Co–S/LIG (a), Raman spectroscopy of C·C, C·C-starch and Ni–Co–S/LIG (b) and EDX spectrum of Ni–Co–S/LIG (c).

the other two. The ratio of $I_G/I_D$ expresses the amount of defects on the LIG and the degree of graphitization.[42] As shown in Table S1,† the $I_G/I_D$ ratio of Ni–Co–S/LIG (1.34) is higher than that of LIG (1.05) and starch-LIG (0.99), which indicates the existence of Ni–Co–S enhancing the degree of graphitization.[43,44]

To obtain the appropriate laser power, LIG was prepared under different power ranging from 2.4 to 7.2 W at the laser scan rate of 9 mm $s^{-1}$. Raman spectroscopy is a powerful tool to obtain crystalline size ($L_a$) along "*a*" axis of graphitic materials by analyzing ratios of the integrated intensities of G and D peaks ($I_G/I_D$).[45] Fig. S3a† shows typical Raman spectra of LIG prepared using laser powers from 2.4 W to 7.2 W. The relationship of the laser power and the $I_G/I_D$ ratio is plotted in the Fig. S3c.† The $L_a$ values are obtained using eqn (1), which is shown in Fig. S3d.† The $I_G/I_D$ ratio and $L_a$ value reach the highest when the laser power is 6.0 W, which are 1.75 and 34 nm, respectively. The higher temperature is beneficial to the surface temperature of the products[46]. However, too high temperature results in generating more D peaks that is not desired.[24] Therefore, 6.0 W is chosen as the proper laser power based on its higher $I_G/I_D$ ratio. Fig. S3b† shows the Raman spectra of Ni–Co–S/LIG with different Co content, and their peaks of D, G, 2D bands and the ratio of $I_G/I_D$ are basically identical (Table S2†).

Typical morphologies of the samples are obtained by measuring FESEM and TEM. The mixture dipping in the carbon cloth contained $Ni^{2+}$ and $Co^{2+}$ that the concentration of $Ni^{2+}$ fixed at 10 mmol $L^{-1}$, while the percent content of $Co^{2+}$ was changed from 2% to 15%. As shown in Fig. S4,† the degree of tightness of Ni–Co–S/LIG increased with smaller interstitials between the Ni–Co–S/LIG particles as the percent content of $Co^{2+}$ increased from 2% to 15%. The typical SEM images of other samples are shown in Fig. 3. There are two differences between LIG and starch-LIG, as shown in Fig. 3a–d. Firstly, the surface of starch-LIG is the smoother than that of LIG. Secondly, the carbon clothes without starch have cracked more seriously than starch-LIG, and the diameter becomes smaller. A possible reason resulting in these two differences is that the carbon cloth was protected by the starch covering above the surface. This is consistent with the results of the Raman spectra shown in Fig. 2b. Furthermore, the surface of LIG and starch-LIG have marked big difference compared to the carbon cloth without laser scribbling (Fig. S5†).

Metal ions mingling in the starch solutions form M-S/LIG (M = Ni or Ni–Co). Obviously, M-S/LIG was quite different than LIG or starch-LIG (Fig. 3). Plenty of particles appear on the surface of the carbon cloth, shown in Fig. 3f and h, which were confirmed as the mixture of $Ni_3S_2$/LIG and $Co_9S_8$/LIG through XRD characterization (Fig. 2a). The appearing of $Co_9S_8$ particles in Ni–Co–S/LIG leads to the surface of Ni–Co–S/LIG denser than that of Ni–S/LIG, since the surface of Co–S/LIG is tighter under the same concentration than Ni content in Ni–S/LIG (Fig. S6†).

Fig. 4 shows the typical TEM, HR-TEM and SAED pattern of Ni–Co–S/LIG. The different magnification of TEM images of Ni–Co–S/LIG are shown in Fig. 4a and b. The dark gray circular particles in the Fig. 4b are confirmed as the Ni–Co–S particles according to Fig. S7,† then the other light colour materials are the LIG. Majority of the of Ni–Co–S particles has a diameter of around 10 nm, as shown in Fig. 4b and e few other particles have the diameter of 25 nm approximately, indicating the Ni–Co–S particles were uniformly prepared. Fig. 4c is representative selected area electron diffraction (SAED) pattern of Ni–Co–S/LIG. The existence of concentric rings indicates the polycrystalline structure, which the rings can be indexed to the (110) and (300) diffractions of rhombohedral phase $Ni_3S_2$. The high-resolution TEM (HRTEM) images of the Ni–Co–S/LIG are shown in Fig. 4d and e. From Fig. 4d, the lattice fringe has 0.33 nm interplanar space, which is ascribed to the (220) plane of LIG corresponding to the light colour region LIG in Fig. 4b and the green colour of Fig. S7b.† As shown in Fig. 4e, the lattice fringe of 0.191 nm and 0.287 nm can be indexed to (511) diffraction of cubic $Co_9S_8$ and (110) diffraction of rhombohedral phase $Ni_3S_2$, respectively, corresponding to the dark gray region Ni–Co–S particles in Fig. 4b. The less intense XRD signal (Fig. 2a) and diffuse concentric rings (Fig. 4c) may be caused by the small particle size and poor polycrystalline structure. The TEM image of Ni–Co–S/LIG and the corresponding elemental mapping are shown in Fig. S8,† with all elements are well distributed in Ni–Co–S/LIG, indicating the high loading of Ni–Co–S particles in LIG. This conclusion can be drawn as well by the EDS spectrum (Fig. S9†).

The detailed information for the surface valence state of elements of as-prepared products was obtained using the X-ray photoelectron spectroscopy (XPS) and the results are shown in Fig. 5 and Fig. S10.† The Ni 2p spectra of XPS is well fitted with

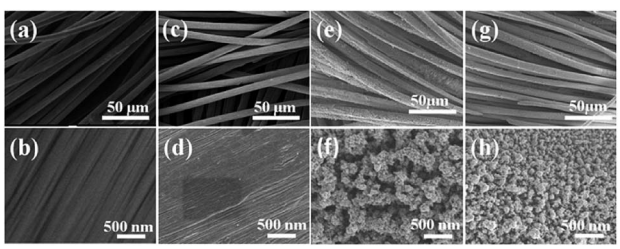


Fig. 3 The SEM images of LIG (a and b), starch-LIG (c and d), Ni–S/LIG (e and f), Ni–Co–S/LIG (g and h).

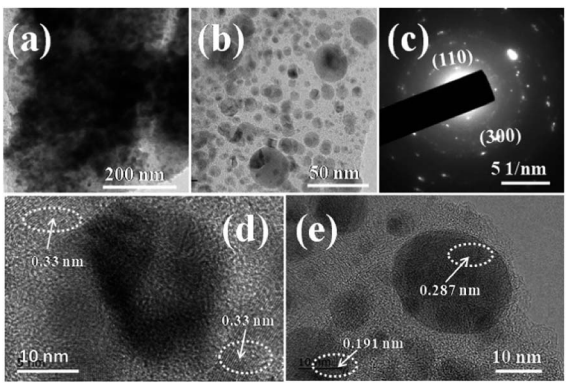


Fig. 4 (a and b) TEM images, (c) the SAED pattern and (d and e) HR-TEM images of Ni–Co–S/LIG.

two spin–orbit splitting, which has doublet characteristics of $Ni^{2+}$ and $Ni^{3+}$. As shown in Fig. 5a, the binding energies of Ni 2p peaks at 856.98 eV and 875.11 eV correspond to $Ni^{2+}$ located in the octahedral sites.[47] The binding energies at 855.55 eV and 873.30 eV can be assigned to $Ni^{3+}$, which located in tetrahedral sites.[48] The intensity of the double peaks is stronger than that of $Ni^{2+}$, indicating $Ni^{3+}$ is the dominant state of Ni near the surface of the sample and comes from $Ni_2S_3$, which is consistent with the XRD analysis. The Co 2p spectrum of XPS is similar to Ni spectra shown in Fig. 5b. The binding energies of stronger peaks at 781.28 eV and 796.38 eV can be assigned to $Co^{3+}$,[47] corresponding to Co 2p3/2 and 2p1/2, respectively. The other spin–orbit doublets locating at 783.60 eV for Co 2p3/2 and 797.57 eV for Co 2p1/2 can be ascribed to $Co^{2+}$.[36] There are two shake-up satellites (denoted as Sat.) existing in both Ni and Co 2p spectra of XPS. The satellite peaks of Co 2p are relatively weak, which is ascribed to the dominance of $Co^{3+}$.[49] Based on the conclusion above, the compositions of as-prepared Ni–Co–S/LIG include $Ni^{2+}$, $Ni^{3+}$, $Co^{2+}$ and $Co^{3+}$, which can contribute as positive materials with high electrochemical property.[50] The S 2p spectra shown in Fig. 5c possesses two peaks round at 162.68 eV for S 2p3/2 and 163.78 eV for S 2p1/2, which correspond to the S in low coordination and metal–sulfur bonds.[48] The O 2p scan is shown in Fig. 5d, and two peaks observing at 532.15 eV and 533.22 eV correspond to O 2p3/2 and 2p1/2, respectively.

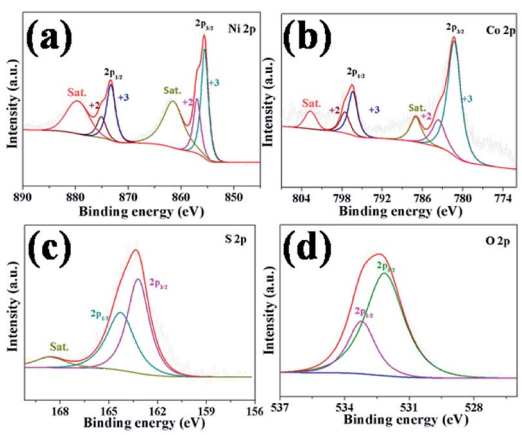


Fig. 5 The XPS spectra of Ni–Co–S/LIG: (a) Ni 2p, (b) Co 2p, (c) S 2p and (d) O 2p.

### 3.2 Electrochemical performance

The electrochemical performances of the different samples prepared at the same conditions were systematically evaluated in a three-electrode system in 2 M KOH aqueous electrolyte. The Ni–Co–S/LIG was served as the working electrode, which the dimension was shown in Fig. S11.† Among the whole electrode, only the square part with the dimension of 10 × 10 mm was immersed in the electrolyte. The CV curves of different as-prepared samples at the scan rate of 10 mV $s^{-1}$ were shown in Fig. 6a, and the potential range is from 0 to 0.6 V. Seen from Fig. 6a, LIG and starch-LIG show a tiny current in comparison to

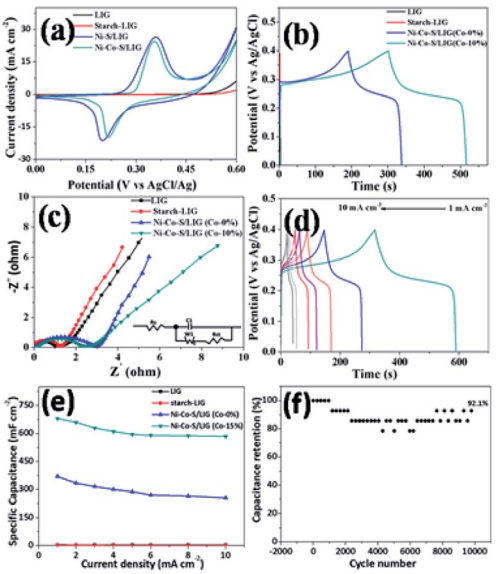


Fig. 6 Electrochemical performance of the different samples for supercapacitors: (a) CV curves of LIG, starch-LIG, Ni–S/LIG and Ni–Co–S/LIG at the scan rate of 10 mV $s^{-1}$, (b) the galvanostatic charge/discharge curves of LIG, starch-LIG, Ni–Co–S/LIG (Co-0%) and Ni–Co–S/LIG (Co-10%) at the current density of 1 mA $cm^{-2}$ (c) the Nyquist plots of LIG, starch-LIG, Ni–Co–S/LIG (Co-0%) and Ni–Co–S/LIG (Co-10%) and the equivalent circuit for modeling Nyquist plots (inset) (d) the galvanostatic charge/discharge curves of Ni–Co–S/LIG (15% Co) (e) the rate performance of the Ni–Co–S/LIG with different Co content (f) cycling performance of the Ni–Co–S/LIG at the current density of 5 mA $cm^{-2}$.

the Ni–S/LIG and Ni–Co–S/LIG, indicating that the contribution of the LIG and starch-LIG towards the capacitance is negligible. It can be observed that Ni–S/LIG and Ni–Co–S/LIG of the CV curves have similar shapes, and exhibit a couple typical redox peaks at about 0.2 V and 0.36 V, which possesses the classical pseudocapacitive nature. Therefore, the specific capacitance is uppermost attributed to the redox reaction with fast and reversible electrochemical processes including $Co^{3+}/Co^{2+}$ and $Ni^{3+}/Ni^{2+}$, which may result from the occurring of reactions shown below[51,52]

$$CoS + OH^- \rightleftharpoons CoSOH + e^-$$

$$CoSOH + OH^- \rightleftharpoons CoSO + H_2O + e^-$$

$$NiS + OH^- \rightleftharpoons NiSOH + e^-$$

The CV curves of Ni–Co–S/LIG have higher current and larger integral areas than that of Ni–S/LIG, illustrating that Ni–Co–S/LIG have higher capacitance. The excellent electrochemical property of Ni–Co–S/LIG may be attributed the addition of the Co element. The CV curves of a series of Ni–Co–S/LIG with different Co content are shown in Fig. S12,† with the scan rates changing from 10 to 100 mV $s^{-1}$. All of the CV curves show typical couple of peaks and the shapes of the CV curves are maintained well along the scan rate rising to 100 mV $s^{-1}$. In addition, the peak current rises/enhances gradually along with

 

the increase of Co content or the scan rate. Obviously, the anodic peaks in CV curves (Fig. S12 a–d†) shift to higher voltage with the increase of Co content at the same scan rate, which consistent with the electrochemical behaviour of Co–S and Ni–S reported previously.[52,53]. Differently, the CV curves of substrate LIG and starch-LIG did not retain original shape with obvious distortion along with the scan rate from 10–100 mV $s^{-1}$ (Fig. S13†) for the polarization.

The GCD curves of the as-prepared samples at the current density of 1 mA $cm^{-2}$ are shown in Fig. 6b. Obviously, the discharge time of Ni–Co–S/LIG is much longer than that of the other three materials, in accordance with the result of CV curves in Fig. 6a. To further evaluate the charge transfer resistance and the diffusive resistance of electrolyte, the electrochemical impedance spectroscopy (EIS) measurement of as-fabricated samples were conducted from 0.1 MHz to 100 MHz, and the results are as shown in Fig. 6c. All the plots show a semicircle and a line appearing in the high and low frequency range, respectively. The diffuse resistance of electrolyte can be calculated from the slope of the curves in the low frequency range, which is defined as the Warburg impedance ($W$). The Ni–Co–S/LIG has small slopes of the straight lines, indicating the high ion diffusion resistance, which may be attributed to the addition of second cobalt ions. The diameter of semi-circle is related to the charge transfer resistance ($R_{ct}$). The large the diameter, the greater the $R_{ct}$. Similar with Warburg impedance, the $R_{ct}$ value of Ni–Co–S/LIG is larger than the others owing to Co ions. The intercept with the $X$-axis at high frequency is related with solution resistance ($R_s$). From Fig. 6c, it can be seen all the samples have small $R_s$. The galvanostatic charge/discharge curves of the Ni–Co–S/LIG were carried out at diverse current densities with the working potential range of 0–0.4 V (Fig. 6d). All the discharge curves at different current densities exhibit the distinct plateau region, which is the characteristic of the typical pseudocapacitive electrode in line with the result of CV curves (Fig. 6a).

The GCD profiles of Ni–Co–S/LIG with different Co content are shown in Fig. S14.† All discharge curves have plateau region, indicating Ni–Co–S/LIG possesses the pseudocapacitive character regardless of the Co content.

The areal specific capacitance of LIG, starch-LIG, Ni–S/LIG and Ni–Co–S/LIG (Co-10%) were calculated to be 4.2, 1.85, 75 and 680 mF $cm^{-2}$ at a low current density of 1 mA $cm^{-2}$, respectively, which was higher than cobalt-based composite.[54] And the capacitance retention rate of Ni–S/LIG and Ni–Co–S/LIG were 73% and 90%, respectively, indicating the increase of capacitance retention with the addition of Co ion. The areal specific capacitance of LIG, starch-LIG, Ni–S/LIG and Ni–Co–S/LIG were calculated from the discharge time and plotted in Fig. 6e at different current density. Ni–Co–S/LIG shows a exceeding large areal specific capacitance of 680 mF $cm^{-2}$, which is 162 times larger than the substrate LIG (4.2 mF $cm^{-2}$) and about 368 times larger than that of starch-LIG (1.85 mF $cm^{-2}$) at the 1 mA $cm^{-2}$. The areal specific capacitance of starch-LIG is lower than LIG, attributing to the protection of starch when the carbon cloth is written using a $CO_2$ laser. Also, Ni–Co–S/LIG has higher capacity than Ni–S/LIG, which may be the synergistic effect of Co ion. The value of areal specific capacitance decreases gradually along with the increasing current density from 1 to 10 mA $cm^{-2}$. It is noteworthy that the capacitance of Ni–Co–S/LIG can reach a capacitive retention of 88.3% at the large current density of 10 mA $cm^{-2}$, which is much higher than that of the substrate LIG (4.2 mF $cm^{-2}$ at 1 mA $cm^{-2}$), starch-LIG (1.85 mF $cm^{-2}$ at 1 mA $cm^{-2}$) and Ni–S/LIG (75 mF $cm^{-2}$ at 1 mA $cm^{-2}$). What is more, Ni–Co–S/LIG has excellent performance compared to a plenty of previously reported LIG-based electrode materials. To the best of our knowledge, such an excellent rate performance has superior to most pseudocapacitor-type electrode materials including carbon materials.[50,52,55–57] The cycling stability of the Ni–Co–S/LIG was further investigated under the GCD process running for 10 000 cycles at a current density of 5 mA $cm^{-2}$, as shown in Fig. 6f. Remarkably, the areal specific capacitance retention can reach *ca.* 92.1% of the initial value after 10 000 cycles, illustrating excellent long-life span cycling stability. And the 92.1% capacitance retention rate is superior to that of many electrode materials reported previously.[52,57,58]

The energy storage of the as-fabricated samples used as electrode materials in the practical application is evaluated to assemble Ni–Co–S/LIG as the positive electrode and active carbon as the negative electrode into the asymmetric MSCs device, as schematically illustrated in Fig. 7a. The mass ratio of Ni–Co–S/LIG and AC is balanced according to the eqn (4) before assembling the asymmetric MSCs device. Take full advantage of the complementary voltage windows ranges of Ni–Co–S/LIG and AC, as shown in Fig. 7b, the working potential of the asymmetric MSCs device can be enlarged to 1.6 V. To search the optimum operating potential window of asymmetric MSCs device, a series of CV measurements at the different potential windows in 2 M KOH electrolyte are conducted, shown in Fig. 7c. Finally 1.6 V is chosen as the maximum voltage window. When the voltage window exceeds 1.6 V, an obvious polarization is observed, which is attributed to the oxygen evolution reaction referring to the secondary reaction.[59,60] As shown in Fig. 7d, all CV curves of the asymmetric MSCs device at various scan rates from 10 to 100 mV $s^{-1}$ at 0–1.6 V are observed a couple of redox peaks appearing, which is ascribed to the reversible redox reaction accompanied with the electrolyte ions insertion/extraction. The shape of CV curve is almost maintained at the high scan rate of 100 mV $s^{-1}$, which illustrates the electrode materials possess excellent rate property as a consequence of fast electronic and ions transportation in the electrode materials. The typical GCD profiles at various current densities ranging from 1 to 10 mA $cm^{-2}$ are shown in Fig. 7e. The plateaus of all the GCD curves are the characteristic of pseudocapacitors, which is in accordance with the CV analysis. The areal specific capacitance is calculated from typical GCD curves at a series of current densities, which is plotted in Fig. 7f. The areal specific capacitance of Ni–Co–S/LIG (Co-10%)//AC asymmetric MSCs device is 160 mF $cm^{-2}$ at the current density of 1 mA $cm^{-2}$, which reaches 141 mF $cm^{-2}$ with the 90.1% of capacitance retention at the current density of 10 mA $cm^{-2}$, higher than that of Ni–Co–S/LIG (Co-0%)//AC asymmetric MSCs device (70.6%).

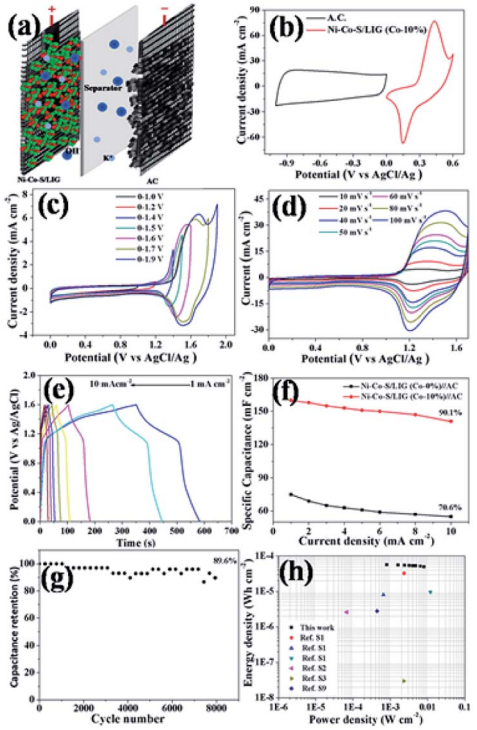


Fig. 7 (a) Schematic illustrations of the assembled Ni–Co–S/LIG//AC asymmetric MSCs device, (b) CV curves of Ni–Co–S/LIG (positive)and AC (negative) at the scan rate of 10 mV $s^{-1}$, (c) CV curves of Ni–Co–S/LIG//AC asymmetric MSCs device in different potential windows at the scan rate of 10 mV $s^{-1}$, (d) CV curves of Ni–Co–S/LIG//AC asymmetric MSCs device at scan rate of 10–100 mV $s^{-1}$, (e) GCD curves of Ni–Co–S/LIG//AC asymmetric MSCs at different current densities (f) the areal specific capacitance of Ni–Co–S/LIG//AC asymmetric MSCs at various current densities, (g) Ragone plots related to energy and power densities of Ni–Co–S/LIG//AC asymmetric MSCs, (h) cycling performance of Ni–Co–S/LIG//AC asymmetric MSCs at a constant current density of 5 mA $cm^{-2}$.

As shown in Fig. S15,† the minor change of *IR* drop at different charge/discharge current densities and the gentle slope can be attributed to small internal resistance and excellent electric and ionic conductivities of the bimetal transition metal sulfides deposited in Ni–Co–S/LIG. Fig. S16† shows that the two asymmetric MSCs devices have small $R_s$. It is a little difference that the $R_{ct}$ value of Ni–Co–S/LIG (Co-0%)//AC asymmetric MSCs is larger than that of Ni–Co–S/LIG (Co-10%)//AC asymmetric MSCs.

The cycling performance of the Ni–Co–S/LIG//AC asymmetric MSCs was investigated at a high current density of 5 mA $cm^{-2}$, and the result was shown in Fig. 7g. It is observed that the long-term cycling stability of the Ni–Co–S/LIG//AC asymmetric MSCs device retains 89.6% of its initial areal specific capacitance after 8000 cycles, which indicates the as-fabricated asymmetric MSCs device possesses desirable cycling stability. Other than some collapse found after 8000 cycles, no obvious change was observed between the morphology of the Ni–Co–S/LIG before and after charging shown in Fig. S17.†

Fig. 7h shows a Ragone plot, illustrating the relationship between the energy density and the power density of Ni–Co–S/LIG//AC asymmetric MSCs device. It can be clearly seen that the areal energy density of the asymmetric MSCs device is 56.9 μW h $cm^{-2}$ at the areal power density of 800 μW $cm^{-2}$. Moreover, an areal energy density of 50.13 μW h $cm^{-2}$ can be obtained at an areal power density of 8000 μW $cm^{-2}$. These results exceed a plenty of previously-reported supercapacitors in literatures (Table S3†), such as LIG-$MnO_2$-MSCs (32.4 μW h $cm^{-2}$ at 2334 μW $cm^{-2}$),[61] LIG-PANI-MSCs (8.0 μW h $cm^{-2}$ at 649 μW $cm^{-2}$),[61] LIG-FeOOH//LIG-$MnO_2$ (9.6 μW h $cm^{-2}$ at 11 853 μW $cm^{-2}$),[61] $MnO_2$/CNT/nylon FSCs (2.6 μW h $cm^{-2}$ at 66.9 μW $cm^{-2}$)[62], LIG (0.8 μW h $cm^{-2}$ at 2290 μW $cm^{-2}$),[61] LIG-$MoS_2$ (2.8 μW h $cm^{-2}$ at 440 μW $cm^{-2}$)[25] just name a few. Hence, the Ni–Co–S/LIG//AC asymmetric MSCs device provides an effective strategy for building high-energy and high-power density asymmetric supercapacitors. To further investigate the practical application, one or two asymmetric MSCs devices can light 17 red and 8 yellow commercial (2.0 V) LEDs, as shown in Fig. S18,† indicating the as-prepared asymmetric MSCs device has high power and energy performance. Obviously, the brightness of three asymmetric MSCs devices lighting the 25 commercial LEDs is higher than that of two asymmetric MSCs devices, which illustrates three asymmetric MSCs devices can store more energy.

## 4 Conclusion

In this work, we have successfully prepared electrode materials comprising of laser-induced 2D graphene integrated with bimetallic Ni–Co–S. This electrode exhibited an outstanding areal specific capacitance of 680 mF $cm^{-2}$ at the current density of 1 mA $cm^{-2}$. Further, an asymmetric MSCs device was fabricated using Ni–Co–S/LIG as positive electrode and active carbon as negative electrode, and it was found that the device has high areal specific capacitance, promising high areal energy density and excellent cycling stabilities. These discoveries not only simplify the preparation of all-in-one bimetallic sulfide integrated with 2D graphene but also exhibit the LDW technique in other pseudocapacitors to obtain the ideal electrode materials.

## Conflicts of interest

The authors declare no conflict of interest.

## Acknowledgements

This work was financially supported by the National Natural Science Foundation of China (No. 21775083), the Research Foundation for Distinguished Scholars of Qingdao Agricultural University (663-1117018).

## References

1 M. Beidaghi and Y. Gogotsi, *Energy Environ. Sci.*, 2014, **7**, 867–884.

2 N. A. Kyeremateng, T. Brousse and D. Pech, *Nat. Nanotechnol.*, 2017, **12**, 7.
3 C. R. Dong, Y. Wang, K. Zhang and H. Zeng, *EnergyChem*, 2020, **2**(1–19), 100026.
4 Q. Jiang, N. Kurra, C. Xia and H. N. Alshareef, *Adv. Energy Mater.*, 2017, **7**, 1601257.
5 W. Liu, W. P. Lustig and J. Li, *EnergyChem*, 2020, **2**(1–35), 100008.
6 Z. L. Wang, *Nano Today*, 2010, **5**, 512–514.
7 D. Yu, K. Goh, H. Wang, L. Wei, W. Jiang, Q. Zhang and Y. Chen, *Nat. Nanotechnol.*, 2014, **9**, 555.
8 J. Chmiola, C. Largeot, P. L. Taberna, P. Simon and Y. Gogotsi, *Science*, 2010, **328**, 480–483.
9 Z. S. Wu, X. Feng and H. M. Cheng, *Natl. Sci. Rev.*, 2013, **1**, 277–292.
10 N. Kurra, B. Ahmed, Y. Gogotsi and H. N. Alshareef, *Adv. Energy Mater.*, 2016, **6**, 1601372.
11 D. Pech, M. Brunet, H. Durou, P. Huang, V. Mochalin, Y. Gogotsi and P. Simon, *Nat. Nanotechnol.*, 2010, **5**, 651–654.
12 J. Lin, C. Zhang, Z. Yan, Y. Zhu, Z. Peng, R. H. Hauge, D. Natelson and J. M. Tour, *Nano Lett.*, 2012, **13**, 72–78.
13 Z. Chen, W. Ren, L. Gao, B. Liu, S. Pei and H. M. Cheng, *Nat. Mater.*, 2011, **10**, 424–428.
14 X. Wang, Y. Zhang, C. Zhi, X. Wang, D. Tang, Y. Xu and Y. Bando, *Nat. Commun.*, 2013, **4**, 2905.
15 K. S. Novoselov, A. K. Geim, S. Morozov, D. Jiang, Y. Zhang, S. Dubonos, I. Grigorieva and A. Firsov, *Science*, 2004, **306**, 666–669.
16 Y. Sun, Q. Wu and G. Shi, *Energy Environ. Sci.*, 2011, **4**, 1113–1132.
17 L. Dai, *Acc. Chem. Res.*, 2012, **46**, 31–42.
18 M. F. El-Kady and R. B. Kaner, *Nat. Commun.*, 2013, **4**, 1475.
19 M. F. El-Kady, V. Strong, S. Dubin and R. B. Kaner, *Science*, 2012, **335**, 1326–1330.
20 H. Tian, H. Y. Chen, T. L. Ren, C. Li, Q. T. Xue, M. A. Mohammad, C. Wu, Y. Yang and H. S. P. Wong, *Nano Lett.*, 2014, **14**, 3214–3219.
21 W. Gao, N. Singh, L. Song, Z. Liu, A. L. M. Reddy, L. Ci and P. M. Aiayan, *Nat. Nanotechnol.*, 2011, **6**, 496.
22 A. M. Dimiev, L. B. Alemany and J. M. Tour, *ACS Nano*, 2012, **7**, 576–588.
23 D. C. Marcano, D. V. Kosynkin, J. M. Berlin, A. Sinitskii, Z. Sun, A. Slesarev, L. B. Alemany, W. Lu and J. M. Tour, *ACS Nano*, 2010, **4**, 4806–4814.
24 J. Lin, Z. Peng, Y. Liu, F. Ruiz-Zepeda, R. Ye, E. L. G. Samuel and J. M. Tour, *Nat. Commun.*, 2014, **5**, 5714.
25 F. Clerici, M. Fontana, S. Bianco, M. Serrapede, F. Perrucci, S. Ferrero and A. Lamberti, *ACS Appl. Mater. Interfaces*, 2016, **8**, 10459–10465.
26 A. Lamberti, F. Clerici, M. Fontana and L. Scaltrito, *Adv. Energy Mater.*, 2016, **6**, 1600050.
27 L. L, J. Zhang, Z. Peng, Y. Li, C. Gao, Y. Ji and H. Fei, *Adv. Mater.*, 2016, **28**, 838–845.
28 Y. Li, D. X. Luong, J. Zhang, Y. R. Tarkunde, C. Kittrell, F. Sargunaraj and J. M. Tour, *Adv. Mater.*, 2017, **29**, 1700496.
29 R. Ye, D. K. James and J. M. Tour, *Acc. Chem. Res.*, 2018, **51**, 1609–1620.
30 P. Simon and Y. Gogotsi, *Acc. Chem. Res.*, 2013, **46**, 1094–1103.
31 K. K. Lee, W. S. Chin and C. H. Sow, *J. Mater. Chem. A*, 2014, **2**, 17212–17248.
32 X. Rui, H. Tan and Q. Yan, *Nanoscale*, 2014, **6**, 9889–9924.
33 W. Li, S. Wang, L. Xin, M. Wu and S. X. Lou, *J. Mater. Chem. A*, 2016, **4**, 7700.
34 J. A. Rajesh, J. H. Park, V. H. V. Quy, J. M. Kwon, J. Chae, S. H. Kang and K. S. Ahn, *J. Ind. Eng. Chem.*, 2018, **63**, 73–83.
35 H. Chen, J. Jiang, L. Zhang, H. Wan, T. Qi and D. Xia, *Nanoscale*, 2013, **5**, 8879–8883.
36 P. Geng, S. Zheng, H. Tang, R. Zhu, L. Zhang, S. Cao and H. Pang, *Adv. Energy Mater.*, 2018, **8**(15), 1703259.
37 Q. Liu, J. Jin and J. Zhang, *ACS Appl. Mater. Interfaces*, 2013, **5**, 5002–5008.
38 C. Zhou, M. Hong, Y. Yang, C. Yang, N. Hu and L. Zhang, *J. Power Sources*, 2019, **438**, 227044.
39 V. Khomenko, E. Raymundo-Pinero and F. Beguin, *J. Power Sources*, 2006, **153**, 183–190.
40 S. P. Singh, Y. Li, A. Beer, Y. Oren, J. M. Tour and C. J. Arnusch, *ACS Appl. Mater. Interfaces*, 2017, **9**, 18238–18247.
41 G. C. A. Gupta, P. Joshi, S. Tadigadapa and P. C. Eklund, *Nano Lett.*, 2006, **6**, 2667–2673.
42 F. Leroux, E. Raymundo-Piñero, J. M. Nedelec and F. Béguin, *J. Mater. Chem.*, 2006, **16**, 2074–2081.
43 S. Peng, L. Li, X. Han, W. Sun, M. Srinivasan, S. G. Mhaisalkar and S. Ramakrishna, *Angew. Chem., Int. Ed.*, 2014, **126**, 12802–12807.
44 Y. Chyan, R. Ye, Y. Li, S. P. Singh, C. J. Arnusch and J. M. Tour, *ACS Nano*, 2018, **12**, 2176–2183.
45 L. G. Cançado, K. Takai, T. Enoki, M. Endo, Y. A. Kim, H. Mizusaki and M. A. Pimenta, *Appl. Phys. Lett.*, 2006, **88**, 163106.
46 S. Kuper, J. Brannon and K. Brannon, *Appl. Phys. A*, 1993, **56**, 43–50.
47 J. Pu, T. Wang, H. Wang, Y. Tong, C. Lu, W. Kong and Z. Wang, *ChemPlusChem*, 2014, **79**, 577–583.
48 J. Xu, P. Gao and T. S. Zhao, *Energy Environ. Sci.*, 2012, **5**, 5333–5339.
49 W. Hu, R. Chen, W. Xie, L. Zou, N. Qin and D. Bao, *ACS Appl. Mater. Interfaces*, 2014, **6**, 19318–19326.
50 L. Huang, D. Chen, Y. Ding, S. Feng, Z. L. Wang and M. Liu, *Nano Lett.*, 2013, **13**, 3135–3139.
51 W. Chen, C. Xia and H. N. Alshareef, *ACS Nano*, 2014, **8**, 9531–9541.
52 L. Yu, L. Zhang, H. B. Wu and X. W. Lou, *Angew. Chem., Int. Ed.*, 2014, **53**, 3711–3714.
53 L. Mei, T. Yang, C. Xu, M. Zhang, L. Chen, Q. Li and T. Wang, *Nano Energy*, 2014, **3**, 36–45.
54 S. S. Zheng, Q. Li, H. G. Xue, H. Pang and Q. Xu, *Natl. Sci. Rev.*, 2020, **7**, 305–314.
55 Y. Xu, Z. Lin, X. Huang, Y. Wang, Y. Huang and X. Duan, *Adv. Mater.*, 2013, **25**, 5779–5784.
56 L. Qie, W. Chen, H. Xu, X. Xiong, Y. Jiang, F. Zou and Y. Huang, *Energy Environ. Sci.*, 2013, **6**, 2497–2504.

57 B. G. Choi, M. Yang, S. C. Jung, K. G. Lee, J. G. Kim, H. Park and Y. S. Huh, *ACS Nano*, 2013, **7**, 2453–2460.
58 S. Peng, L. Li, C. Li, H. Tan, R. Cai, H. Yu and Q. Yan, *Chem. Commun.*, 2013, **49**, 10178–10180.
59 S. J. Peng, L. L. Li, H. B. Wu, S. Madhavi and X. W. Lou, *Adv. Energy Mater.*, 2015, **5**, 1401172.
60 J. Zhao, Z. J. Li, M. Zhang, A. L. Meng and Q. D. Li, *J. Power Sources*, 2016, **332**, 355–365.
61 L. Li, J. Zhang, Z. Peng, Y. Li, C. Gao, Y. Ji and H. Fei, *Adv. Mater.*, 2016, **28**(5), 838–845.
62 C. Choi, S. H. Kim, H. J. Sim, J. A. Lee, A. Y. Choi, Y. T. Kim and S. J. Kim, *Sci. Rep.*, 2015, **5**, 1–6.

 